Aero-optical measurements in a subsonic, turbulent boundary layer with non-adiabatic walls

Stanislav Gordeyev, Jacob A. Cress, Adam Smith, and Eric J. Jumper

Citation: Physics of Fluids (1994-present) **27**, 045110 (2015); doi: 10.1063/1.4919331
View online: http://dx.doi.org/10.1063/1.4919331
View Table of Contents: http://scitation.aip.org/content/aip/journal/pof2/27/4?ver=pdfcov
Published by the AIP Publishing

PHYSICS OF FLUIDS **27**, 045110 (2015)

Aero-optical measurements in a subsonic, turbulent boundary layer with non-adiabatic walls

Stanislav Gordeyev,[1,a)] Jacob A. Cress,[2,b)] Adam Smith,[1] and Eric J. Jumper[1]
[1]*University of Notre Dame, Notre Dame, Indiana 46556, USA*
[2]*GE Aviation, Cincinnati, Ohio 45215, USA*

(Received 27 January 2015; accepted 30 March 2015; published online 29 April 2015)

This paper presents experimental studies of aero-optical distortions due to a turbulent boundary layer over a range of subsonic speeds with the underlying wall both heated above and cooled below the adiabatic wall temperature. A statistical scaling model, based on extended strong Reynolds analogy is derived and shown to correctly predict experimentally observed results. The temperature mismatch between the flow and the wall was shown to have a profound effect on the level aero-optical aberrations, as the heated wall amplifies them and the cooled wall significantly reduces distortions. The importance of an inclusion of the pressure term in explaining the boundary-layer density fluctuations with the cooled wall is also discussed. © *2015 AIP Publishing LLC*. [http://dx.doi.org/10.1063/1.4919331]

I. INTRODUCTION

The aero-optic problem is concerned with the study of wavefront aberrations caused by a variable index-of-refraction turbulent flow over an optical aperture.[1–4] Free-shear layers, compressible boundary layers, shocks, and mixed density flows are potential sources for aero-optical aberrations,[1,3] as index-of-refraction variations, n', are related to density fluctuations, ρ', as $n' = K_{GD}\rho'$, where K_{DG} is a Gladstone-Dale constant;[5] for air and visible wavelengths, it is approximately 2.27×10^{-4} m^3/kg. When a collimated laser beam with a planar (i.e., in-phase) wavefront is projected through the variable index-of-refraction field, the emerging beam's wavefront will be distorted. These wavefront aberrations can potentially have a severe negative effect on the performance of an optical system, be it for free-space communication, imaging, or directed-energy applications.[3] When the propagation length is relatively short, the levels of wavefront distortions can be quantified by Optical-Path-Length, $OPL(x,y,t)$,[2]

$$OPL(x,y,t) = \int_a^b n'(x,y,z,t)dz = K_{GD}\int_a^b \rho'(x,y,z,t)dz,$$

where the integration is performed along the beam propagation axis, z, the primes denote fluctuating components, and spatial distributions are given on a (x,y)-plane normal to the z-axis. A spatially averaged mean is commonly subtracted from OPL and defined as Optical-Path-Difference, OPD, $OPD(x,y,t) = OPL(x,y,t) - \langle OPL(x,y,t)\rangle$, where the angular brackets denote the spatial average in the (x,y)-plane. Typically, the spatial root-mean-square of OPD at each instant in time, $OPD_{rms}(t)$, and the time-averaged spatial root-mean-square of OPD, OPD_{rms}, are computed.

The effect that wavefront aberrations have on an optical system is typically quantified with the time-averaged Strehl ratio, $\overline{SR}$, which is defined as $\overline{SR} = I/I_0$, where I is the instantaneous intensity

a)Author to whom correspondence should be addressed. Electronic mail: sgordeye@nd.edu
b)This work was performed while the author was a graduate student at the Department of Aerospace and Mechanical Engineering, University of Notre Dame, Indiana 46556, USA.

on the optical axis and I_0 is the diffraction limited, distortion-free intensity value. The time-averaged Strehl ratio can be approximated using the $\mathrm{OPD}_{\mathrm{rms}}$ value and the "large-aperture approximation,"[6,7]

$$\overline{SR} = \exp\left[-\left(\frac{2\pi \mathrm{OPD}_{\mathrm{rms}}}{\lambda}\right)^2\right], \tag{1}$$

where λ is the laser wavelength.

Many different optical-system configurations have been envisioned: most employing an external turret that is exposed to the flow or an enclosed beam steering mirror with the aperture flush to the aircraft skin. The first configuration must contend with a complex flow field due to the presence of the turret in flow,[8] while the latter configuration only has the aircraft's turbulent boundary layer over the aperture.[9]

Turbulent boundary layers have been the subject of aero-optical research since the early 1950s, primarily concerned with the crispness of Schlieren photographs.[3,10,11] One consequence of this work was the prospect of using the optical aberration measurements as a method of inferring turbulent scales. Sutton[12] derived a theoretical formulation for the aberration effect of turbulent boundary layers based upon statistical measures of the turbulence. This "linking equation" between turbulence quantities and OPD_{rms} is, in a simplified form, given as

$$OPD_{rms}^2 = 2K_{GD}^2 \int_0^L \rho_{rms}^2(y)\Lambda_\rho(y)\,dy, \tag{2}$$

where ρ_{rms} is the root-mean-square density profile, and Λ_ρ is the density correlation length. The linking equation, Eq. (2), has been validated both experimentally[9,13] and numerically.[14,15] Equation (2) establishes a relation between the level of aero-optical distortions and properties of the density structure, ρ_{rms} and Λ_ρ. So, aero-optical data can provide important information about the density fields in turbulent flows.

Through the 1960s and 1970s, aero-optical studies of turbulent boundary layers intensified due to an interest in placing optical systems on aircraft. Both direct measurements using interferometry[16] and indirect measurements using hot-wires to estimate the density fluctuations[17] were conducted. With aero-optical distortions caused by boundary layers being found to be generally less than a micrometer, turbulent boundary layers were initially thought to have little or no impact of the optical system performance.[3] However, as follows from Eq. (1), for a fixed value of $\mathrm{OPD}_{\mathrm{rms}}$, decreasing the laser wavelength will have the effect of decreasing the time-averaged Strehl ratio. Optical systems being considered today use near infrared and visible wavelengths ($\sim$1 μm), which have an order of magnitude shorter wavelength than the CO_2 laser used in 1970s. While the small impact on the far-field beam intensity of the turbulent boundary layer was not previously a factor in the design of optical systems, this drastic reduction in wavelength can now cause the boundary layer to have a discernable influence on overall system performance.[18,19]

Advances in wavefront sensors, primarily in the Malley probe and Shack-Hartmann sensors, combined with various advanced data reduction algorithms, allow collecting spatially- and temporally resolved wavefronts with very good accuracy. The use of the Malley probe in making optical measurements in turbulent subsonic boundary layers has shown to give the most accurate and highly time-resolved information about optical distortions with bandwidths >100 kHz.[9] Recently, wavefront sensors, called Shack-Hartmann sensors, based on high-speed digital cameras were shown to provide comparable or even better sampling speeds and accuracy.[9,20,21] It was found that for subsonic speeds, optical distortions were proportional to the boundary layer displacement thickness, the freestream density, and the square of the freestream Mach number, $\mathrm{OPD}_{\mathrm{rms}} \sim \delta^*\rho M^2$,[9] consistent with earlier measurements.[16,17,22] It was also found in these studies that optical distortions convect at speeds of 0.82 of the freestream speed and the typical scale of aero-optical distortions is on the order of the boundary-layer thickness.[9] These results strongly suggest that optically active structures reside in the outer portion of the boundary layer. Experimental studies of aero-optical distortions caused by supersonic boundary layers were also performed, and the scaling law was extended to supersonic speeds.[23,24]

Most of the studies cited above have not previously accounted for the potential temperature mismatch between the underlying wall and freestream temperature, so the study described in this paper experimentally investigated the impact that heat transfer at the underlying wall of a subsonic, compressible, turbulent boundary layer has on optical aberrations.

Wyckham and Smits[24] used a high-speed two-dimensional Shack-Hartmann sensor to study aero-optical properties of subsonic and supersonic boundary layers. Although they did not perform heated wall experiments, they used a bulk-flow analysis and developed a scaling law for aero-optical aberrations for non-adiabatic walls as a function of the freestream Mach number, the local skin friction coefficient, C_f, and the ratio of the freestream static temperature, T_∞, to the wall temperature, T_w,

$$\mathrm{OPD}_{\mathrm{rms}} \sim K_{GD}\delta M_\infty^2\sqrt{C_f}\left(\frac{T_w}{T_\infty}+1\right)^{-3/2}. \tag{3}$$

From this scaling law, it follows that aero-optical distortions should decrease when the wall is heated. These predictions contradicted the preliminary experimental studies conducted in Ref. 25, where it was shown that aero-optical distortions increase when the wall is heated. White and Visbal[26] have performed large eddy simulations of aero-optic aberrations caused by compressible turbulent boundary layers for heated and cooled walls and also have shown that aero-optical aberrations increased when the wall was heated. So, there is a need for a statistical model for the $\mathrm{OPD}_{\mathrm{rms}}$ as a function of subsonic Mach number and moderate temperature difference between the wall and the freestream.

The model is derived in Sec. II. The experimental set-up and data reduction technique are presented in Sec. III. The theoretical relationship is compared against experimental data from both heated and cooled wall experiments in Sec. IV, followed by conclusions and a discussion of the temperature mismatch implications in Sec. V.

II. AERO-OPTICAL MODEL FOR SUBSONIC BOUNDARY LAYER WITH NON-ADIABATIC WALL

A. Extended strong Reynolds analogy

For nearly as long as turbulent boundary layers have been studied, those with a moderate heat transfer at the wall have been the subject of experimental and computational research, especially applied to supersonic and hypersonic boundary layers; see Refs. 27 and 28 for summaries of the effects of heat transfer in a compressible, turbulent boundary layer. A significant advancement in the field came in 1962 from Morkovin's presentation of the Strong Reynolds Analogy (SRA),[29] which presumes that p' is negligible. From this analogy between the Reynolds-averaged form of the energy and momentum equations, a relationship between the fluctuating static temperature and fluctuating velocity can be shown to be

$$\frac{T_{rms}}{\bar{T}} = -(\gamma-1)\,M^2\frac{u_{rms}}{\bar{U}}, \tag{4a}$$

where T is the static temperature, γ is the specific heat ratio, $\bar{U}$ and u are the mean and fluctuating components of the local streamwise velocity, respectively, $M = \bar{U}/a$ is a local Mach number, a is the local speed of sound, and an overbar indicates mean quantities. Note that Eq. (4a) is strictly valid only when the Prandtl number is unity. The SRA, consistent with the assumption that p' is approximately zero, neglects fluctuations in the total temperature in a boundary layer. While the total temperature fluctuations for turbulent boundary layers were found to be on the same order of magnitude as the static temperature fluctuations,[30,31] Eq. (4) was still found to be approximately valid for adiabatic-wall boundary layers,

$$\frac{T_{rms}}{\bar{T}} = -A(y)\,(\gamma-1)\,M^2\frac{u_{rms}}{\bar{U}}, \tag{4b}$$

where $A(y)$, shown in Figure 8, takes into account the stress integral distribution in the boundary layer,[27] in the original SRA $A(y) = 1$. Both experiments[27,32,33] and DNS simulations[31,34] have shown that $A(y) \approx 1$ for $y/\delta < 0.6$ and increases in the outer layer.

However, for non-adiabatic wall conditions, experimental[30] and computational[34,35] studies have shown that SRA fails to predict the correct temperature fluctuations. Walz[36] proposed a form of the enthalpy equation such that $\tilde{h} = h(\tilde{u})$, where fluctuations in the total temperature are not ignored,[27] and the following relationship for mean static temperature was found:

$$\frac{\tilde{T}}{T_\infty} = \frac{\tilde{T}_w}{T_\infty} + \frac{\tilde{T}_r - \tilde{T}_w}{T_\infty}\left(\frac{\tilde{U}}{U_\infty}\right) - r\frac{(\gamma-1)}{2}M_\infty^2\left(\frac{\tilde{U}}{U_\infty}\right)^2, \tag{5a}$$

where $\tilde{T}$, $\tilde{T}_\infty$, $\tilde{T}_w$, and $\tilde{T}_r$ are the Favre-averaged static, freestream, wall, adiabatic, and recovery temperatures, respectively, $\tilde{U}$ is the Favre-averaged mean velocity, M_∞ is the freestream Mach number, and $r = (\tilde{T}_r - \tilde{T}_\infty)/(\tilde{T}_{0_\infty} - \tilde{T}_\infty)$ is the recovery factor. In turbulent boundary layers with air as the fluid in motion, r is typically about 0.89. Equation (5a) is known by several names: the modified Crocco relation, the Walz equation, or the Extended SRA (ESRA).

Linearizing this equation in the case of small fluctuations,[30] a relation between temperature and velocity fluctuations becomes

$$\frac{T''_{rms}}{T_\infty} = \frac{\tilde{T}_r - \tilde{T}_w}{T_\infty}\left(\frac{u''_{rms}}{U_\infty}\right) - r(\gamma-1)M_\infty^2\frac{\tilde{U}u''_{rms}}{U_\infty^2}, \tag{5b}$$

where T''_{rms} and u''_{rms} are the Favre-averaged fluctuating temperature and velocity, respectively. For an adiabatic wall, this equation becomes Eq. (4b) with $A(y) = r$. Cebeci and Smith[37] derived a very similar expression with $A(y) = 1$.

The difference between Reynolds and Favre-averaging has been shown to be less than 1.5% for Mach numbers less than three;[27] thus, Reynolds-averaging will be used in the remainder of the paper.

In Ref. 31, the results of DNS simulations of the compressible supersonic boundary layer showed that while the total temperature fluctuations are of the same order of magnitude as the static temperature fluctuations, Eq. (5b) is still approximately valid due to a particular relationship between the total and the static temperature fluctuations. A similar conclusion was drawn in Ref. 34, where direct numerical simulations of a hypersonic boundary layer with different wall temperatures were performed. They also numerically verified that Eq. (5a) is valid within 10%.

While ESRA gives comparable results for wall-normal locations between the wall and half of the boundary layer thickness, $y < 0.5\delta$,[34] comparing Eq. (4b) and Eq. (5b) and numerical results from Ref. 34 suggest that, in general, Eq. (5b) can be written in the following form:

$$\frac{T_{rms}}{T_\infty} = \frac{T_r - T_w}{T_\infty}\left(\frac{u_{rms}}{U_\infty}\right) - A(y)(\gamma-1)M_\infty^2\frac{Uu_{rms}}{U_\infty^2}. \tag{5c}$$

Strictly speaking, Eq. (5c) simply postulates the relationship between $T_{\rm rms}$ and $u_{\rm rms}$, while ESRA, in addition to Eq. (5c), also requires that the temperature and velocity fluctuations are perfectly anti-correlated. This was shown not to be true, see, for example, Refs. 30, 31, 34, and 38.

B. Model for non-adiabatic boundary-layer aero-optical distortions

From Eq. (2), it follows that if the density fluctuations and their correlation lengths across the boundary layer are known, optical distortions can be calculated. From the ideal gas law, $p = \rho RT$, the density fluctuations, ρ', are related to pressure fluctuations, p', and temperature fluctuations, T'. In the case of small fluctuations, it can be written as $\rho'/\rho(y) = p'/p(y) - T'/T(y)$. While the pressure fluctuations in adiabatic boundary layers have been shown to be several times smaller than the temperature fluctuations,[14,27,28] for cooled walls, the temperature fluctuations are smaller than in the adiabatic case.[34] So, the pressure fluctuations can be comparable with the temperature fluctuations.

Using Eqs. (5a) and (5c), letting $\Delta T = T_w - T_r$, and replacing fluctuating values with root-mean-square values, the following expression for $T_{\rm rms}$ can be found:

$$\left(\frac{T_{\rm rms}}{T_\infty}\right)^2 = \left(\frac{u_{\rm rms}}{U_\infty}\right)^2 \cdot \left[\left(\frac{\Delta T}{T_\infty}\right)^2 + 2A(y)(\gamma-1)M_\infty^2\left(\frac{\Delta T}{T_\infty}\right)\frac{U}{U_\infty} + \left(A(y)(\gamma-1)M_\infty^2\frac{U}{U_\infty}\right)^2\right], \quad (6)$$

where $U(y)$ is the mean local streamwise velocity. Thus, the equation of state can be used to compute the density fluctuations, assuming no correlation between the pressure and temperature (we will discuss this assumption later),

$$\left(\frac{\rho_{\rm rms}}{\rho(y)}\right)^2 = \left(\frac{T_{\rm rms}}{T(y)}\right)^2 + \left(\frac{p_{\rm rms}}{P_\infty}\right)^2. \quad (7)$$

Here, the local pressure is assumed to be constant across the boundary layer. The local density can be found from the equation of state, $\rho(y) = P_\infty/(RT(y)) = \rho_\infty(T_\infty/T(y))$, where the mean temperature profile can be computed from Eq. (5a),

$$\frac{T(y)}{T_\infty} = 1 + r\frac{(\gamma-1)}{2}M_\infty^2\left(1 - \left[\frac{U(y)}{U_\infty}\right]^2\right) + \frac{\Delta T}{T_\infty}\left(1 - \frac{U(y)}{U_\infty}\right). \quad (8a)$$

For non-adiabatic boundary layers, the fluctuating velocity component, compensated for density changes near the wall using the Van Driest transformation, $\frac{u_{rms}}{u_\tau}\sqrt{\frac{\rho(y)}{\rho_w}}$, was found to be mostly unchanged over a wide range of Mach numbers,[28,31,34] so a fluctuating velocity profile from the adiabatic boundary layer[31] can be used,

$$\frac{u_{rms}(y)}{u_\tau}\sqrt{\frac{\rho(y)}{\rho_w}} = \frac{u_{rms}(y)}{U_\infty\sqrt{C_f/2}}\sqrt{\frac{\rho(y)}{\rho_\infty}} = \frac{u_{rms}(y)}{U_\infty\sqrt{C_f/2}}\sqrt{\frac{T_\infty}{T(y)}} = g(y/\delta). \quad (8b)$$

We further assume that the mean velocity profile is independent of the wall temperature as

$$U(y)/U_\infty = f(y/\delta). \quad (8c)$$

Finally, the fluctuating pressure profile from Ref. 31 will be used,

$$p_{rms}/(\rho_w u_\tau^2) = p_{rms}/(\rho_w U_\infty^2(C_f/2)(\rho_\infty/\rho_w)) = p_{rms}/(\rho_\infty U_\infty^2(C_f/2)) = h(y/\delta), \quad (8d)$$

where the functions f, g, and h are presented in Figure 8. Substituting Eq. (6) into Eq. (7) and using Eqs. (8b)-(8d) gives the following relationship for $\rho_{\rm rms}$ in terms of the velocity, and the temperature profiles in the wall normal direction for a given ΔT yields

$$\left(\frac{\rho_{\rm rms}}{\rho_\infty}\right)^2 = \left(\frac{T_\infty}{T(y)}\right)^2\left[\left(\frac{T_{\rm rms}}{T(y)}\right)^2 + \left(\frac{p_{\rm rms}}{P_\infty}\right)^2\right] = \left(\frac{T_{\rm rms}}{T_\infty}\right)^2\left(\frac{T_\infty}{T(y)}\right)^4 + \left(\frac{T_\infty}{T(y)}\right)^2\left(\frac{p_{\rm rms}}{P_\infty}\right)^2 =$$
$$\left(\frac{T_\infty}{T(y)}\right)^3(C_f/2)g^2(y)\cdot\left[\frac{\Delta T}{T_\infty} + A(y)(\gamma-1)M_\infty^2 f(y)\right]^2 + \left(\frac{T_\infty}{T(y)}\right)^2\left[\gamma M_\infty^2(C_f/2)h(y)\right]^2. \quad (9)$$

Finally, substituting Eq. (9) into Eq. (2) results in the following relationship:

$${\rm OPD}_{\rm rms} = A_0 K_{GD}\rho_\infty\delta\sqrt{C_f}\left[M_\infty^4 + C_1\frac{\Delta T}{T_\infty}M_\infty^2 + C_2\left(\frac{\Delta T}{T_\infty}\right)^2\right]^{1/2}, \quad (10)$$

where

$$A_0^2 = \int_0^\infty [(\gamma-1)A(y)f(y)g(y)]^2 (T_\infty/T(y))^3 \Lambda(y)dy + \gamma^2 (C_f/2) \int_0^\infty g^2(y)h^2(y)(T_\infty/T(y))^2\Lambda(y)dy,$$

$$C_1 = 2(\gamma-1)\int_0^\infty A(y)f(y)g^2(y)(T_\infty/T(y))^3\Lambda(y)dy/A_0^2,$$

$$C_2 = \int_0^\infty g^2(y)(T_\infty/T(y))^3\Lambda(y)dy/A_0^2.$$

Note that for the adiabatic wall boundary layer, i.e., $\Delta T = 0$, Eq. (10) reduces to the experimentally proven[9,23] scaling relation, $\mathrm{OPD}_{\mathrm{rms}} \sim \rho_\infty \delta \sqrt{C_f} M_\infty^2$.

From Eq. (10), $\mathrm{OPD}_{\mathrm{rms}}^2$ is a quadratic function of ΔT and reaches a minimum at

$$\frac{\Delta T_{\min}}{T_\infty M_\infty^2} = -\frac{C_1}{2C_2} = -\frac{(\gamma-1)\int_0^\infty A(y)f(y)g^2(y)(T_\infty/T(y))^3\Lambda(y)dy}{\int_0^\infty g^2(y)(T_\infty/T(y))^3\Lambda(y)dy}, \tag{11a}$$

with a value of

$$\frac{OPD_{rms}^2(\Delta T_{\min})}{OPD_{rms}^2(\Delta T=0)} = \frac{\int_0^\infty \left(g^2(y)\cdot(T_\infty/T(y))\left[A(y)(\gamma-1)M_\infty^2 f(y) - \frac{\Delta T_{\min}}{T_\infty}\right]^2 + \gamma^2(C_f/2)h^2(y)\right)(T_\infty/T(y))^2\Lambda(y)dy}{A_0^2}. \tag{11b}$$

For positive ΔT, Eq. (10) can be rearranged in the following manner:

$$\mathrm{OPD}_{\mathrm{rms}} = A_0 K_{GD}\rho_\infty\delta\sqrt{C_f}\left(M_\infty^2 + D_1\frac{\Delta T}{T_\infty}\right)\left[1 + \frac{D_2}{2}\left(\frac{\Delta T/T_\infty}{M_\infty^2 + D_1\Delta T/T_\infty}\right)^2 + H.O.T.\right], \tag{12}$$

where $D_1 = C_1/2$ and $D_2 = C_2 - (C_1/2)^2$. For positive temperature differences, the second term in the square brackets in Eq. (12) will be shown to be much smaller than unity and Eq. (10) can be further simplified as

$$\mathrm{OPD}_{\mathrm{rms}} = A_0 K_{GD}\rho_\infty\delta\sqrt{C_f}\left(M_\infty^2 + D_1\frac{\Delta T}{T_\infty}\right), \quad \Delta T > 0. \tag{13}$$

Several important conclusions can be drawn from analyzing the model predictions.

1. Cooling the wall to $\Delta T_{\min}$ should significantly reduce the aero-optical distortions.
2. Amount of cooling, $\Delta T_{\min}$, is proportional to a square of the freestream Mach number.
3. $\Delta T_{\min}/(T_\infty M_\infty^2)$ primarily depends on the choice of $A(y)$.
4. Finally, heating the wall will increase the aero-optical distortions.

In summary, the model provides testable predictions about choices for $A(y)$ and $\Lambda(y)$, and comparing experimental results to the model predictions should provide the evidence to support (albeit indirectly) a particular choice of both $A(y)$ and Λ.

III. EXPERIMENTAL SET-UP AND DATA REDUCTION

In order to test the model predictions for $A(y)$ and $\Lambda(y)$, fluidic and aero-optical boundary layer measurements over a range of Mach numbers between 0.2 and 0.5 were conducted in an indraft transonic tunnel at the Hessert Laboratory for Aerospace Research at the University of Notre Dame. The wind tunnel, shown in Figure 1, has an open circuit configuration with a

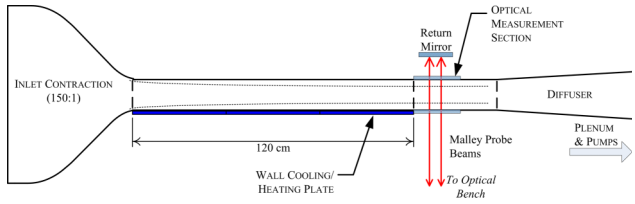

FIG. 1. Schematic of the indraft transonic tunnel with a heated/cooled boundary layer.

150:1 contraction ratio. Velocity is varied by controlling the pressure in the plenum, which is located just downstream of the diffuser section. The boundary layer test section has a cross section measuring 9.9 cm × 10.1 cm, with a development length of 155 cm from the contraction to the measurement station. During experiments, the freestream velocity was monitored directly using a pitot-static probe. The boundary layer profile was measured with a single boundary-layer hotwire at several locations along the test section between x = 13 cm and x = 156 cm. Velocity profiles were measured along the bottom tunnel wall at 100 kHz for 5 s at each point in the profile, and the anemometer's built-in low-pass filter was used with a cutoff frequency of 50 kHz. The hot wire was calibrated in the freestream for Mach numbers ranging from M = 0.16 to 0.43, and the freestream Mach number for each test was set at M = 0.4. At the measurement station, x = 170 cm, the boundary layer thickness, δ, was 2.4 cm, the displacement thickness, δ^*, was 3.6 mm, and the momentum thickness, Θ, was found to be 2.75 mm. The shape factor, $H = \delta^*/\Theta$, for the boundary layer was 1.3, which agrees well with values for zero-pressure-gradient boundary layers at this Re_Θ.[39] For a range of tested subsonic Mach numbers between 0.2 and 0.6, a Reynolds number range based on the momentum thickness, $\mathrm{Re}_\Theta = U_\infty\Theta/\upsilon$, was between 12 000 and 35 000 at the test station and the Reynolds number range based on the development length x = 170 cm, was approximately $(7.6–21.1) \times 10^6$.

For non-adiabatic wall experiments, one wall of the boundary layer development section was replaced with an aluminum plate, see Figure 1. To create a heated boundary layer, flexible, electric resistive coil heaters were epoxied to the outside surface of the aluminum plate and insulated. The temperature of the heaters was controlled with a proportional integral differential (PID) circuit with the temperature input coming from a thermal sensor embedded flush to the inside wall which measured the wall surface temperature. The thickness of the aluminum plate was 5 mm to ensure a uniform wall surface temperature. Wall temperature was directly measured using thermocouples embedded in the aluminum plate in order to provide accurate wall temperature measurements over the length of the test section. For the heated wall experiments, Mach numbers of 0.2, 0.3, 0.4, and 0.5 were tested. Several wall temperatures were tested at each Mach number; it should be noted that due to the fixed output power of the electric heaters, the maximum achievable wall temperature was dependent on the flow speed, with a greater difference between the freestream and the wall temperature achieved at Mach 0.2 ($\Delta T \sim 28\,^\circ$C) than at Mach 0.5 ($\Delta T \sim 15\,^\circ$C).

To study the boundary layer with the cooled wall, the sidewalls of the boundary layer development test sections were constructed of 3/8 in. thick. Aluminum plates and reservoirs were installed on the outside of the wind tunnel in order to provide cooling to these portions of the side wall. The side walls of the boundary layer development section were cooled using dry ice while the wind tunnel was off, taking care to make sure the walls were uniformly cooled. Both walls were instrumented with thermocouples at x = 20, 60, and 100 cm to accurately measure the wall temperature over the length of the test section. After reaching a significantly low temperature (typically around −30 °C), the dry ice was removed and the tunnel was switched on. Once the freestream velocity reached a steady state, simultaneous wall-temperature, free-stream velocity, and wavefront measurements were obtained as the tunnel wall temperature increased to the recovery wall temperature, T_r. Three Mach numbers were tested: 0.35, 0.4, and 0.5, and different temperature differences were achieved at each Mach number.

Wavefront measurements of the subsonic boundary layers were acquired using the Malley Probe, which uses two or more parallel small-diameter (~1 mm) beams, separated in the direction of

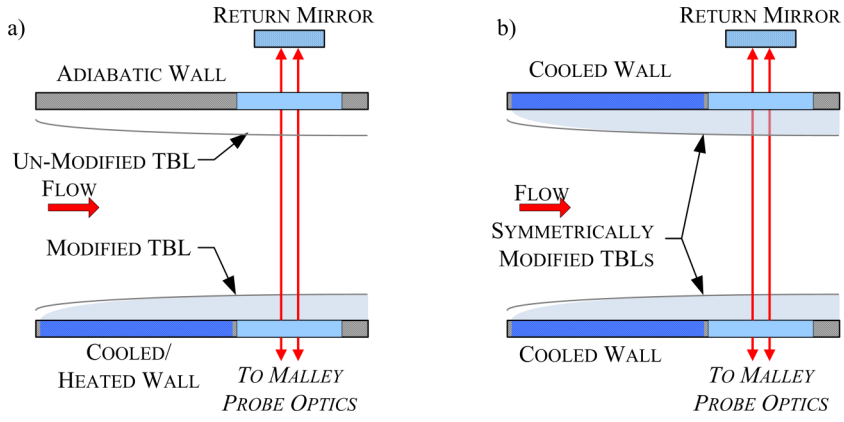

FIG. 2. Schematic of the experimental set-up for (a) single-modified boundary layer (SMBL) and (b) double-modified boundary layer (DMBL).

flow by some distance, Δ. The Malley probe provides direct measurements of levels of aero-optical distortions, OPD_{rms}, the convective velocity, and the streamwise correlation length. The reader is referred to Ref. 9 for further information and a discussion of the Malley probe setup, operation, and data analysis, so only essential details are given here.

The beam from He-Ne laser was re-collimated and split into two small parallel beams, separated in the streamwise direction; the beam separation was varied between 6 and 11 mm for different runs. The beams were then propagated into the test section normal to the optical window, as shown in Figure 2. The return mirror on the other side of the test section reflected beams back to the optical bench along the same optical path. The returning beams were split off using a cube beam splitter and each beam was focused onto a Position Sensing Device (PSD), capable of measuring instantaneous beam deflections, $\theta(t)$. The sampling frequency was 100 kHz with a typical sampling time of 15 s.

Wall cooling was applied to either just one side of the wind tunnel test section or to both sides, as illustrated in Figures 2(a) and 2(b), respectively. Note that in both of these cases, the Malley probe beams pass through both boundary layers and therefore measures the aero-optic aberrations from both boundary layers. This is known as the double-boundary-layer (DBL) measurement technique, and it has been shown previously[40,41] that the DBL-measured $(OPD_{rms})^2$ can be considered as a linear combination of $(OPD_{rms})^2$ from the individual boundary layers,

$$\left(OPD^2_{rms}\right)_{DBL} = \left(OPD^2_{rms}\right)_1 + \left(OPD^2_{rms}\right)_2,$$

where the subscripts 1 and 2 denote the wavefront statistics from the first and second boundary layers, respectively. In the case where the boundary layers are statistically identical, as shown in Figure 2(b), the above relation reduces to the following form:

$$\left(OPD^2_{rms}\right) = \frac{1}{2}\left(OPD^2_{rms}\right)_{DBL}.$$

If one boundary layer is modified by cooling/heating the wall, as shown in Figure 2(a), the OPD_{rms} of the cooled/heated boundary layer can be determined from the measurement of both the adiabatic and cooled/heated boundary layers, labeled as SMBL, see Figure 2(a),

$$\left(OPD_{rms}\right)_{Cooled} = \sqrt{\left(OPD^2_{rms}\right)_{SMBL} - \frac{1}{2}\left(OPD^2_{rms}\right)_{DBL,Adiabatic}},$$

where the subscript "DBL, Adiabatic" denotes the measurement of two symmetric, adiabatic boundary layers at the same location, and Mach number. This relation was shown to work well for extracting wavefront statistics for heated boundary layers.[41]

For wall-cooling experiments, wavefronts were acquired primarily using the single modified boundary layer method; however, wavefronts for double-modified boundary layers were also acquired at $M = 0.4$ in order to validate the single modified boundary layer method.

A. Malley probe 1-D wavefront data reduction

For the Malley probe, data were acquired as time series of the streamwise beam deflection angles, $\theta(t)$, and the mean value of the deflection angle for each beam was removed. Assuming that the flow is "frozen" and convecting with the convection velocity U_C, OPD can be computed from time series of deflection angle measurements, $\mathrm{OPD}\,(x = -U_c t) = -U_c \int_0^t \theta\,(t)\,dt$, and the spatial root-mean-squared value of the wavefront, OPD_{rms}, was computed, Equivalently,[9] OPD_{rms} can be computed from the deflection angle spectrum,

$$OPD^2_{rms} = 2U_C \int_0^\infty \frac{|\hat{\theta}(f)|^2}{(2\pi f)^2} df. \tag{14}$$

The convective speed is calculated from the spectral cross-correlation between the beams.[9]

Although the Malley probe measures only 1-dimensional slices of wavefronts, independent 2-dimensional wavefront measurements performed on the same boundary layer using a high-speed Shack-Hartmann sensor[9] and numerical simulations of the turbulent boundary layer[14,15] confirmed that the Malley probe correctly measures $\mathrm{OPD}_{\mathrm{rms}}$, wavefront correlation lengths, and other wavefront statistical properties.

An example of the deflection angle spectrum is shown in Figure 3(a). The spectrum has a peak around $St_\delta = f\delta/U_\infty \sim 1$, implying that a dominant source of aero-optical distortions is a large, on the order of the boundary layer thickness, structure. The increase of the spectrum at low frequencies, $St_\delta < 0.1$, is due to contamination from mechanical vibration of optical components in the experiment. These mechanical-related vibrations were high-pass filtered before calculating $\mathrm{OPD}_{\mathrm{rms}}$. Sharp peaks at the high-end of the spectrum are related to electronic interference and were also removed from the signal.

By cross-correlating beams, the convective velocity is experimentally calculated from the argument, or the phase of the cross-correlation, $S(f) = \langle \hat{\theta}_1(f)\hat{\theta}_2^*(f)\rangle$.[9] The typical phase plot is presented in Figure 3(b), showing a linear frequency dependence of the phase over a large frequency domain. Knowing the phase slope, the convective speed can be calculated as $U_C = \Delta/\tau$ for two beams separated by some distance, Δ, where τ is computed from the slope of the argument as $d\mathrm{Arg}[S(f)]/df = 2\pi\tau$. The convective speed of the canonical boundary-layer aero-optical structures was found to be 0.82 of the freestream speed for subsonic speeds, in agreement with previous measurements, mentioned in the Introduction.

If the deflection angle spectrum exhibits self-similarity for different temperature differences, from Eq. (14), it follows that for the same boundary layer thickness and Mach number,

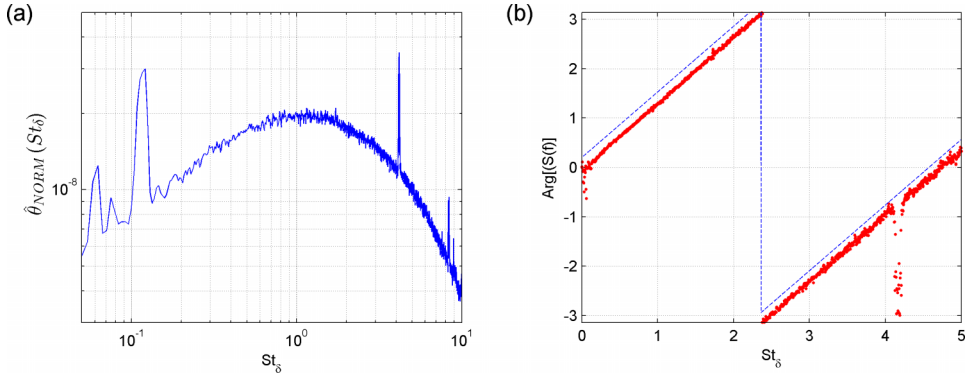

FIG. 3. (a) Typical boundary-layer Malley probe deflection angle amplitude spectrum and (b) the cross-correlation phase plot, where data are shown as dots and a linear fit, shifted for clarity, is shown as a dashed line. Reprinted with permission from S. Gordeyev, A. E. Smith, J. A. Cress, and E. J. Jumper, "Experimental studies of aero-optical properties of subsonic turbulent boundary layers," J. Fluid Mech. **740**, 214 (2014). Copyright 2014, Cambridge University Press.

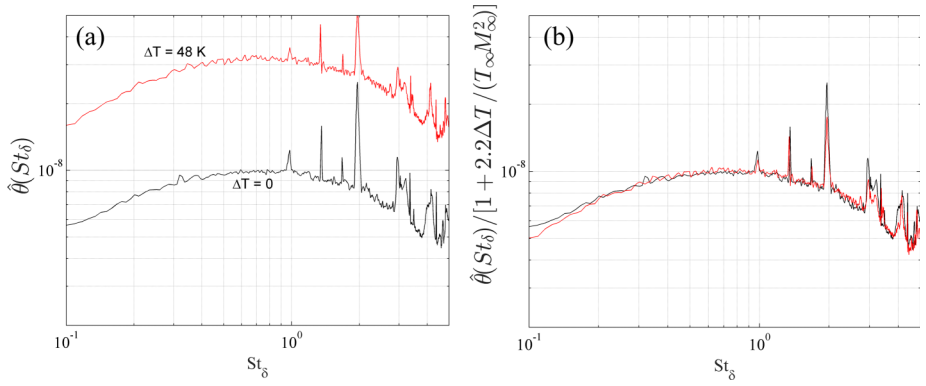

FIG. 4. (a) Deflection angle spectra, neglecting the temperature dependence (i.e., $D_1 = 0$), for the Mach 0.4 turbulent boundary layer at two ΔT extremes, 0 and 48 K. (b) Deflection angle spectra, normalized with temperature dependence using Eq. (13). Sharp peaks in the high end of the spectra are noise-related.

$$\hat{\theta}(f) \sim OPD_{rms}. \tag{15}$$

Thus, the amplitude of the deflection angle spectrum has the same functional form on the wall temperature as OPD_{rms}.

IV. RESULTS

A. Heated wall

From Eqs. (13) and (15), it follows that the deflection angle spectrum for the heated boundary layer should be simply amplified by the term $\left(M_\infty^2 + D_1(\Delta T/T_\infty)\right)$, but its shape should be unchanged. Figure 4(a) shows the unscaled deflection angle amplitude spectra at Mach 0.4 for two temperature differences, $\Delta T = 0$ and 48 K. Figure 4(b) shows the normalized deflection angle spectra for the same conditions but including the temperature difference in the normalization, Eq. (13); the procedure of calculating D_1 from the experimental data is discussed in the next paragraph. The proposed normalization for the temperature dependence shows an excellent collapse of the experimental data. The location of the peak spectrum value near $St_\delta \sim 1$ is not affected by the change in temperature difference, and moreover, the shape of the spectrum was not altered, but rather it was just linearly shifted vertically with ΔT. This suggests that the effect of temperature difference, at least in the regime studied, did not significantly change the overall statistical properties of the boundary layer structures, but only amplified the fluctuating density values within the structures. Also, the spectrum was linearly amplified across a large range of St_δ values, which suggests that the temperature difference equally affected a broad range of structure sizes.

To determine the value of the D_1 constant, Eq. (13) can be re-arranged as

$$\frac{OPD_{rms}(\Delta T) - OPD_{rms}(\Delta T = 0)}{OPD_{rms}(\Delta T = 0)} = D_1 \frac{\Delta T}{T_\infty M_\infty^2}. \tag{16}$$

To compute OPD_{rms} for both the heated and the cooled boundary layers, the deflection angle time history signal was high-pass filtered above $St_\delta = 0.1$, integrated via Eq. (14) and the effect of the second boundary layer over the unheated wall was removed, as discussed before, to calculate OPD_{rms} values for the single heated boundary layer. Constants D_1 were computed from Eq. (16) for all Mach numbers using a linear regression. The extracted values of D_1 are plotted versus Re_Θ in Figure 5. The constant does not appear to be a function of the Reynolds number, at least in the studied range. The mean value of D_1 was found to be $D_1 = 2.13 \pm 0.07$, giving the experimental value of $C_1 = 2D_1 = 4.22 \pm 0.14$.

Figure 6 shows the OPD_{rms} data for the heated wall experiments plotted versus the linear scaling relationship in Eq. (13). The linear scaling relationship successfully collapses OPD_{rms} values over a wide range of subsonic Mach numbers and positive temperature differences. The slope of the

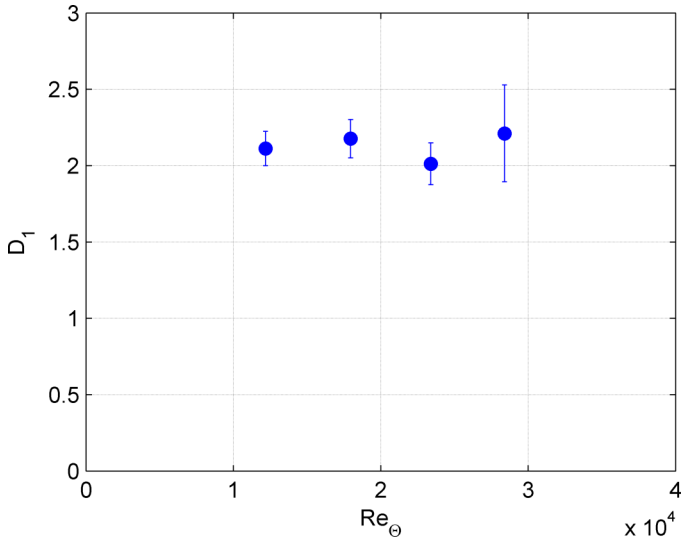

FIG. 5. D_1 versus Re_Θ for the heated boundary layer.

OPD_{rms} data was found to be $A_0 = 0.19$, which is consistent with the previously reported value of 0.2 for adiabatic boundary layers.[9] Further, it is apparent from these results that a positive mismatch between the wall temperature and the adiabatic wall temperature can greatly affect the OPD_{rms} value that an optical system would experience. Thus, the effect of positive temperature difference cannot be ignored in optical measurements of the turbulent boundary layer.

B. Cooled wall

For negative temperature differences, the full scaling relationship, Eq. (10), should be used. Factoring out M_∞^2 from the right hand side of Eq. (10) gives the normalized OPD_{rms} expression,

$$\frac{OPD_{rms}(\Delta T)}{OPD_{rms}(\Delta T = 0)} = \left[1 + C_1 \frac{\Delta T}{(T_\infty M_\infty^2)} + C_2 \left(\frac{\Delta T}{(T_\infty M_\infty^2)}\right)^2\right]^{1/2}. \tag{17}$$

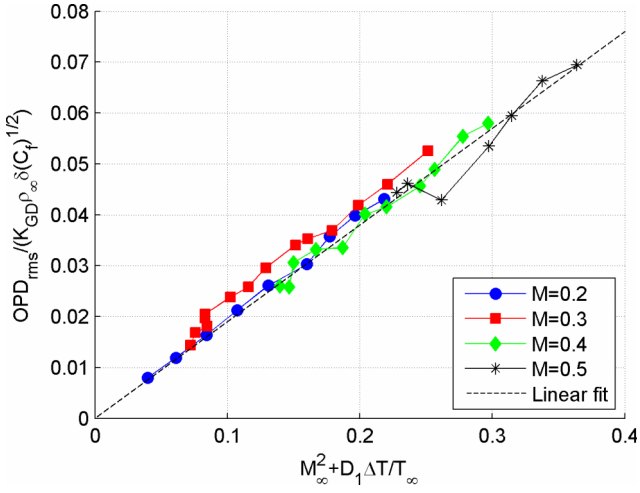

FIG. 6. Normalized OPD_{rms} versus $(M_\infty^2 + D_1(\Delta T/T_\infty))$ for all Mach numbers and positive temperature differences.

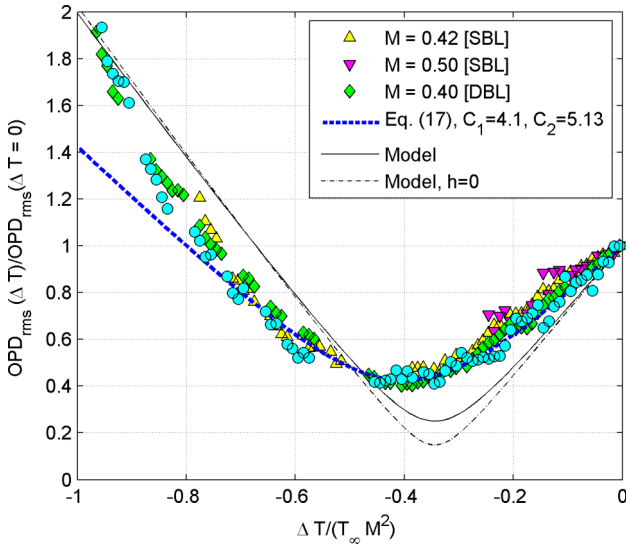

FIG. 7. OPD_{rms} normalized by the OPD_{rms} value with $\Delta T = 0$ versus $\Delta T/\left(T_\infty M_\infty^2\right)$, the best-fit using Eq. (17), and the model predictions, Eq. (10), using $\Lambda_1(y)$ and $A(y)$ from Figure 8 with and without the pressure term.

As discussed earlier, for negative temperature differences, given in Eq. (11a), aero-optical distortions should be at their minimum. The normalized OPD_{rms} data for three Mach numbers are plotted versus $\Delta T/\left(T_\infty M_\infty^2\right)$ in Figure 7, and the strong effect of the difference between the wall and adiabatic wall temperature is apparent in this figure. Results of both SBL and DBL experiments agree with each other, confirming the validity of the data extraction outlined in Sec. III. All experimental results successfully collapse onto one curve, and the minimum of approximately 0.4 in the normalized OPD_{rms} value is clearly observed around $\Delta T/\left(T_\infty M_\infty^2\right) = -0.4$. In other words, the optical aberrations in the turbulent boundary layer were decreased by 60% at this temperature difference. This is a dramatic decrease in the magnitude of optical aberrations, and it provides a promising passive way to significantly reduce aero-optical distortions caused by turbulent boundary layers. The results also confirm the model prediction that the modest wall cooling reduces OPD_{rms}. Performing a least-square fit, the constants C_1 and C_2 were found to be 4.1 and 5.13, respectively. Equation (17) with these constants is plotted in Figure 7, showing a fairly good prediction of the normalized OPD_{rms}-values for the range of $\Delta T/\left(T_\infty M_\infty^2\right)$ between 0 and −0.7; below −0.7, experimental results are higher than what Eq. (17) predicts, indicating a possible departure from some of

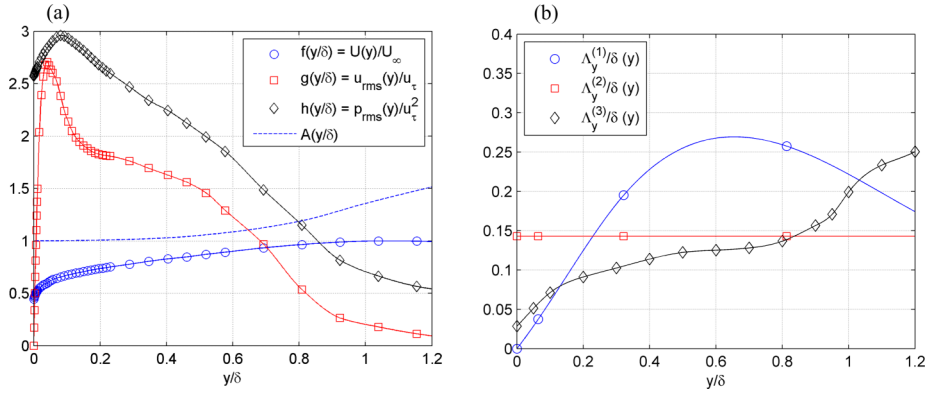

FIG. 8. (a) Normalized mean (measured), u_{rms} velocity profiles (from Ref. 31), p_{rms} profile (from Ref. 31), and $A(y)$ (from Ref. 27) used to evaluate constants in the model, Eq. (10). (b) Different choices of the density correlation lengths are from Refs. 14, 16, and 17, respectively.

the assumptions used in deriving the model. The value of C_1 agrees within experimental error with the one obtained from the heated-wall experiment. Also, the second term in Eq. (12) is always less than $D_2/(2D_1^2) = 0.03$, verifying the assumption made in deriving Eq. (13).

The model requires the knowledge of the velocity profile, Eqs. (8b) and (8c), the pressure fluctuation profile, Eq. (8d), the function $A(y)$, defined in Eq. (5c), and the density correlation length, $\Lambda(y)$. The mean velocity profile was measured using the hot-wire at $M_\infty = 0.4$, while the fluctuation velocity and pressure profiles are taken from the DNS simulations;[31] these profiles are presented in Figure 8(a). Three different choices of the density correlation lengths were used and shown in Figure 8(b): Λ_1 measured in Ref. 16, Λ_2 from Ref. 17, and Λ_3 from numerical simulations in Ref. 14. For the A-function, three choices are tested: $A(y) = r$, $A(y) = 1$, and $A(y)$, taken from Ref. 27, and shown in Figure 8(a).

Table I presents values of A_0, C_1, C_2, $\Delta T_{\min}/(T_\infty M_\infty^2)$, and $OPD_{rms}(\Delta T_{\min})/OPD_{rms}(\Delta T = 0)$, predicted by the model for different selected $A(y)$ and $\Lambda(y)$. Using results from Table I, the closest prediction of the experimentally measured values of C_1, C_2, the location, and the value of the minimum OPD_{rms} is given with Λ_1 or Λ_3 and $A(y)$ shown in Figure 8. Theoretical predictions with and without the pressure term are also shown in Figure 7. The theoretical model predicts the location of the minimum OPD_{rms} for $\Delta T_{\min}/(T_\infty M_\infty^2) = -0.34$, which is within 15% of the experimentally observed value. The theoretical model underpredicts the minimum value of OPD_{rms} by 30%. One possible source for this discrepancy is that in deriving the model, the cross-term $\langle T'p' \rangle$ was not included. However, this term is not negligible, as the temperature fluctuations are partially due to the total temperature fluctuations,[30,31] which are, in turn, the consequence of the pressure fluctuations. So, the inclusion of the cross-term would most probably increase the level of density fluctuations and would result in higher values of OPD_{rms}.

The model supports the choice of $A(y)$ shown in Figure 8, as all other choices lead to even smaller values of $\Delta T_{\min}/(T_\infty M_\infty^2)$, see Table I. Notice that the choice of Λ does not significantly affect $\Delta T_{\min}/(T_\infty M_\infty^2)$.

Figure 7 also shows the importance of including the pressure term into the model, as without it, the model predicts a much lower value of 0.17 for $OPD_{rms}(\Delta T_{\min})/OPD_{rms}(\Delta T = 0)$. Notice that the inclusion of the pressure term is important only in the temperature range of the lowest OPD_{rms} and does not significantly alter OPD_{rms} for the canonical adiabatic-wall boundary layer. As discussed earlier, it is generally accepted that in adiabatic-wall boundary layers, the temperature fluctuations are several times larger than the pressure fluctuations, so the pressure fluctuations can be neglected. But from the presented model, Eq. (6), it follows that in the moderately cooled boundary layers, the temperature fluctuations are suppressed, while the pressure fluctuations, which are related to velocity fluctuations, are not significantly modified. Thus, the cooled-wall boundary layer might be a better suitable flow to study the pressure fluctuations inside the boundary layer.

A final comment about the pressure term in the model is that its relative importance is proportional to C_f, see Eq. (11b), and it would be even more important at low Reynolds numbers.

As mentioned in the Introduction, the only other model for including temperature effects to predict aero-optical distortions of a boundary-layer is the model proposed in Ref. 24 and given

TABLE I. Various parameters predicted by the model.

A(y)	$\Lambda(y)$	A_0	C_1	C_2	$\frac{\Delta T_{\min}}{T_\infty M_\infty^2}$	$\frac{OPD_{rms}(\Delta T_{\min})}{OPD_{rms}(\Delta T=0)}$	$\frac{OPD_{rms}(\Delta T_{\min})}{OPD_{rms}(\Delta T=0)}$, $h=0$
$= r$	Λ_1	0.17	6.41	10.99	−0.29	0.25	0.10
$= r$	Λ_2	0.15	6.84	12.69	−0.27	0.27	0.14
$= r$	Λ_3	0.13	6.59	11.73	−0.28	0.27	0.12
$= 1$	Λ_1	0.19	5.77	8.80	−0.33	0.23	0.10
$= 1$	Λ_2	0.17	6.17	10.18	−0.30	0.27	0.14
$= 1$	Λ_3	0.15	5.94	9.41	−0.32	0.25	0.12
From Figure 8	Λ_1	0.20	5.46	7.92	−0.34	0.25	0.14
From Figure 8	Λ_2	0.18	5.91	9.44	−0.31	0.27	0.17
From Figure 8	Λ_3	0.15	5.63	8.54	−0.33	0.27	0.17

in Eq. (3). From their model, it follows that optical aberrations are inversely related to the wall temperature; their model predicts that the value of OPD_{rms} will *decrease* as the wall temperature is *increased*. Clearly, the experimental data presented in this paper pointedly contradict this result. A close inspection shows that the model from Ref. 24 is based upon the SRA, not the "extended" SRA, and assumes that total enthalpy is constant throughout the boundary layer and therefore does not allow the total temperature to vary.

C. Convective speeds at different wall temperatures

The presented model, Eq. (9), estimates the boundary-layer density profile for different wall temperatures. One can make a plausible assumption that the density structure convects at the local velocity, and the observed overall convective speed of the aero-optical structure is related to the velocity integral weighted by the density field. So, we can speculate that the measured convective speed of aero-optical structures can be presented as

$$\frac{U_C}{U_\infty} = \frac{\int |\rho_{rms}(y,\Delta T)|\, f(y/\delta) dy}{\int |\rho_{rms}(y,\Delta T)|\, dy}. \tag{18}$$

It is worth noting that the similar approach was used to correctly predict the experimentally observed increase in the convective speed of aero-optical structures in a boundary layer at supersonic speeds.[25] The model prediction, Eq. (18), with $A(y)$ from Figure 8, is plotted in Figure 9 as a function of the wall temperature, along with experimental measurements of the convective speeds. While the particular choice of the integral in Eq. (18) is admittedly somewhat *ad hoc*, the model properly predicts all the experimentally observed trends, including the reduction of the convective speed for large negative $\Delta T/\left(T_\infty M_\infty^2\right) < -0.5$ and even absolute values of the convective speed for the adiabatic wall boundary layer. From the model, one can see that for large negative temperature differences, the mean temperature profile near the wall, Eq. (8a), was modified, compared to the adiabatic wall case. This led to the increase of the density fluctuations near the wall, while in the outer part of the boundary layer, the density fluctuations were still suppressed. Therefore, the slower-moving structures near the wall were optically "amplified," leading to the decrease in the overall convective speed of aero-optical structure. The model prediction without the inclusion of the pressure term is also shown in Figure 9 and shows a lesser agreement with the data. Thus, it also indicates that the pressure term has to be included to study density fluctuations in moderately cooled boundary layers.

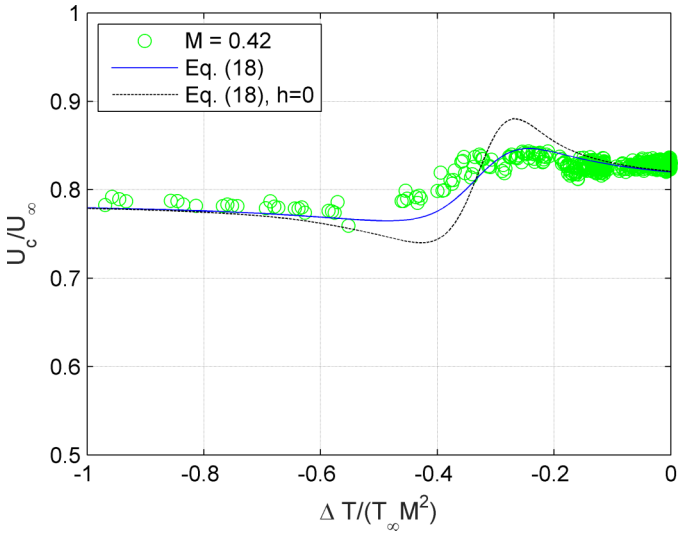

FIG. 9. Convective speed of aero-optical structure as function of the wall temperature.

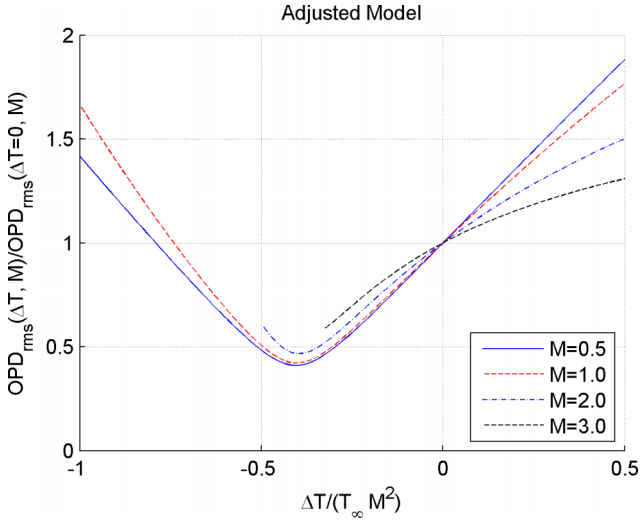

FIG. 10. Adjusted model predictions (with Λ_1 and $A(y)$ from Figure 8) at subsonic and supersonic speeds.

D. Extension to supersonic speeds

The model reasonably predicts all the important aero-optical characteristics of non-adiabatic-wall subsonic boundary layers; it also correctly predicts OPD_{rms} for supersonic adiabatic boundary layers.[23] Because the density correlation lengths[42] and normalized pressure variations[43] are similar for subsonic and supersonic speeds, the model predictions can be extended to the supersonic non-adiabatic regime. Results of the predicted levels of OPD_{rms} at different Mach numbers and temperature differences, *adjusted to match experimental results at subsonic speeds*, are shown in Figure 10. At supersonic speeds, the OPD_{rms}-level becomes a non-linear function of the wall temperature for the heated boundary layer, and the relative increase in OPD_{rms} becomes less pronounced for Mach numbers larger than one. OPD_{rms} still has a minimum value around $\Delta T/\left(T_\infty M_\infty^2\right) = -0.4$ for all Mach numbers; also the relative reduction in OPD_{rms} is similar for both subsonic and supersonic boundary layers. Note that for $M_\infty = 2.0$ and $M_\infty = 3.0$, the lines in Figure 10 do not extend to large negative temperatures because the wall temperature eventually reaches the absolute zero and cannot be cooled further.

Overall, the wall cooling still should be an effective way to reduce aero-optical distortions of the boundary layer at low supersonic speeds, $M_\infty < 3$. The optimal cooling is expected to be around $\Delta T/\left(T_\infty M_\infty^2\right) = -0.4$ with the reduction in OPD_{rms} by a factor of 2 or so.

V. CONCLUSIONS AND DISCUSSION

The primary objective of this paper is to present a theoretical model for the fluctuating density field in adiabatic, cooled, and heated boundary layers based on the extended strong Reynolds analogy. The fluctuating density field, in turn, can be used to predict the aero-optical distortions in adiabatic- and non-adiabatic-wall boundary layers. Strictly speaking, the model presented here does not require a perfect anti-correlation between the velocity and the temperature fluctuations but rather simply assumes a functional dependence between them. The experimental data described in the paper were collected specifically to validate the theoretical model; these data were used to test predictions for heated- and cooled-wall experiments at several subsonic Mach numbers. The wall temperature effect on OPD_{rms} was successfully predicted by the model. For a heated wall, the data validated the model's prediction that the level of aero-optical distortion is a linear function of $\Delta T/\left(T_\infty M_\infty^2\right)$. For the cooled wall boundary layer, aero-optical distortions initially decrease with a negative $\Delta T/\left(T_\infty M_\infty^2\right)$, reach a minimum value at $\Delta T/\left(T_\infty M_\infty^2\right) = -0.4$, and finally increase for larger negative temperature differences; this behavior was also successfully predicted by the model.

By assuming different relations between the velocity and the temperature fields and comparing the theoretical predictions with the experimental results, the particular functional dependence between the velocity and the temperature fields was generally supported. In addition, the comparison demonstrated that the pressure term should be included to explain the density fluctuations for the moderately cooled boundary layers. The model also correctly predicts the variation in the aero-optical convective speed for cooled walls. Finally, the model predictions for different temperature differences were extended to supersonic speeds.

Aero-optical distortions are directly linked to the density structure by the linking equation, Eq. (2), so studying these aero-optical distortions gives many important insights into the properties of the density field in boundary layers, which is a hard quantity to measure experimentally. Also, by varying the wall temperature, the temperature field can be modified independently from the pressure field and their respective effects on the density field can be accurately and non-intrusively measured.

The work presented in this paper shows that a heat addition or subtraction at the wall in a subsonic, compressible turbulent boundary layer has an important impact on the optical aberration imprinted on the wavefront of a laser propagated through the boundary layer. Particularly, it implies that the aircraft skin upstream of the optical aperture should be kept close to or below the recovery temperature; otherwise, any airborne system which requires optical propagation through the boundary layer will experience larger values of aero-optical distortions. Using cooled walls, aero-optical distortions might be decreased by as much as 60%, providing potentially important practical means to passively mitigate aero-optical effects in boundary layers.

From the deflection angle spectra, it is apparent that for the range of ΔT values tested, a moderate ΔT from the heated wall simply amplifies the density fluctuations in the boundary layer with little or no effect on the velocity statistics of the boundary layer. Further, the amplitude in the deflection angle spectrum varied linearly with the temperature difference. Thus, increasing the wall temperature will not alter the aero-optical structure, but rather will simply amplify it optically, at least in the temperature range tested. These results suggest that low speed flows with very low levels of optical aberrations can be made optically active by introducing a temperature mismatch between the wall and freestream; therefore, optical aberrations that are unobservable at $\Delta T = 0$ can be measured with the same optical wavefront instruments without distorting the relevant structures by simply heating the wall. One consequence of this result is the possibility of using non-intrusive optical diagnostic tools, like a Malley probe or a high-speed wavefront sensor, to study boundary layers in low speed turbulent boundary layer facilities. This result greatly increases the number of turbulent boundary layer facilities that can be used in aero-optic research, as well as allows sensitive optical sensors to be used to study turbulent boundary layers at low subsonic speeds; this has already led to a development of new experimental approaches to study fundamental physics of boundary layers.[44]

ACKNOWLEDGMENTS

This work is supported by the Air Force Office of Scientific Research, Grant Nos. FA9550-09-1-0449 and FA9550-12-1-0060. The U.S. Government is authorized to reproduce and distribute reprints for governmental purposes notwithstanding any copyright notation thereon.

[1] K. G. Gilbert and L. J. Otten, *Aero-Optical Phenomena*, Progress in Astronautics and Aeronautics Series Vol. 80 (American Institute of Aeronautics and Astronautics, New York, 1982).
[2] M. Wang, A. Mani, and S. Gordeyev, "Physics and computation of aero-optics," Annu. Rev. Fluid Mech. **44**, 299-321 (2012).
[3] E. J. Jumper and E. J. Fitzgerald, "Recent advances in aero-optics," Prog. Aerosp. Sci. **37**(3), 299-339 (2001).
[4] E. J. Fitzgerald and E. J. Jumper, "The optical distortion mechanism in a nearly incompressible free shear layer," J. Fluid Mech. **512**, 153-189 (2004).
[5] J. H. Gladstone and T. P. Dale, "Researches on the refraction, dispersion, and sensitiveness of liquids," Philos. Trans. R. Soc. London **153**, 317-343 (1863).
[6] T. S. Ross, "Limitations and applicability of the Maréchal approximation," Appl. Opt. **48**(10), 1812-1818 (2009).
[7] C. Porter, S. Gordeyev, and E. Jumper, "Large-aperture approximation for not-so-large apertures," J. Opt. Eng. **52**(7), 071417 (2013).
[8] S. Gordeyev and E. Jumper, "Fluid dynamics and aero-optics of turrets," Prog. Aerosp. Sci. **46**, 388-400 (2010).
[9] S. Gordeyev, A. E. Smith, J. A. Cress, and E. J. Jumper, "Experimental studies of aero-optical properties of subsonic turbulent boundary layers," J. Fluid Mech. **740**, 214-253 (2014).

[10] H. W. Liepmann, "Deflection and diffusion of a light ray passing through a boundary layer," Report No. SM-14397, Douglas Aircraft Company, Santa Monica Division, California, 1952.
[11] H. A. Stine and W. Winovich, "Light diffusion through high-speed turbulent boundary layers," NACA Research Memorandum, NACARMA-56B21, Washington, 1956.
[12] G. W. Sutton, "Effect of turbulent fluctuations in an optically active fluid medium," AIAA J. **7**(9), 1737-1743 (1969).
[13] R. J. Hugo and E. J. Jumper, "Applicability of the aero-optic linking equation to a highly coherent, transitional shear layer," Appl. Opt. **39**(24), 4392-4401 (2000).
[14] K. Wang and M. Wang, "Aero-optics of subsonic turbulent boundary layers," J. Fluid Mech. **696**, 122-151 (2012).
[15] K. Wang and M. Wang, "On the accuracy of malley probe measurements of aero-optical effects: A numerical investigation," J. Opt. Eng. **52**(7), 071407 (2013).
[16] K. G. Gilbert, "KC-135 aero-optical boundary-layer/shear-layer experiments," *Aero-Optical Phenomena*, Progress in Astronautics and Aeronautics Vol. 80, edited by K. G. Gilbert and L. J. Otten (AIAA, New York, 1982), pp. 306-324.
[17] W. C. Rose, "Measurements of aerodynamic parameters affecting optical performance," Air Force Weapons Laboratory Final Report, AFWRL-TR-78-191, 1979.
[18] S. Gordeyev, J. Cress, and E. Jumper, "Far-field laser intensity drop-outs caused by turbulent boundary layers," J. Dir. Energy **5**(1), 58-75 (2013).
[19] K. G. Gilbert, "Challenges of high-brightness laser systems: A photon Odyssey," Opt. Eng. **52**(7), 071412 (2013).
[20] A. E. Smith, S. Gordeyev, and E. J. Jumper, "Recent measurements of aero-optical effects caused by subsonic boundary layers," J. Opt. Eng. **52**(7), 071404 (2013).
[21] A. E. Smith, S. Gordeyev, H. Ahmed, A. Ahmed, D. J. Wittich, and M. Paul, "Shack-hartmann wavefront measurements of supersonic turbulent boundary layers in the TGF," AIAA Paper No. 2014–2493, 2014.
[22] B. Masson, J. Wissler, and L. McMackin, "Aero-optical study of a NC-135 fuselage boundary layer," AIAA Paper No. 94–0277, 1994.
[23] S. Gordeyev, E. Jumper, and T. Hayden, "Aero-optical effects of supersonic boundary layers," AIAA J. **50**(3), 682-690 (2012).
[24] C. Wyckham and A. Smits, "Aero-optic distortion in transonic and hypersonic turbulent boundary layers," AIAA J. **47**(9), 2158-2168 (2009).
[25] J. Cress, S. Gordeyev, and E. Jumper, "Aero-optical measurements in a heated, subsonic, turbulent boundary layer," AIAA Paper No. 2010-0434, 2010.
[26] M. D. White and M. R. Visbal, "Aero-optics of compressible boundary layers in the transonic regime," AIAA Paper No. 2012-2984, 2012.
[27] A. J. Smits and J. P. Dussauge, *Turbulent Shear Layers in Supersonic Flow* (American Institute of Physics, Woodbury, New York, 1996), Chap. 5.
[28] E. F. Spina, A. J. Smits, and S. K. Robinson, "The physics of supersonic turbulent boundary layers," Annu. Rev. Fluid Mech. **26**, 287-319 (1994).
[29] M. V. Morkovin, "Effects of compressibility on turbulent flows," in *Mechanique de la Turbulence*, edited by A. Favre (CNRS, Paris, France, 1962), pp. 367-380.
[30] J.-F. Debieve, P. Dupont, D. R. Smith, and A. J. Smits, "Supersonic turbulent boundary layer subject to step changes in wall temperature," AIAA J. **35**(1), 51-57 (1997).
[31] S. E. Guarini, R. D. Moser, K. Shariff, and A. Wray, "Direct numerical simulations of a supersonic turbulent boundary layer at Mach 2.5," J. Fluid Mech. **414**, 1-33 (2000).
[32] J. Debiève, "Etude d'une interaction turbulence onde de choc," Ph.D. thesis, Thèse Université d'Aix Marseille II, 1983.
[33] D. R. Smith and A. J. Smits, "Simultaneous measurement of velocity and temperature fluctuations in the boundary layer of supersonic flow," Exp. Therm. Fluid Sci. **7**, 221-229 (1993).
[34] L. Duan, I. Beekman, and M. P. Martin, "Direct numerical simulation of hypersonic turbulent boundary layers. 2. Effect of wall temperature," J. Fluid Mech. **655**, 419-445 (2010).
[35] K. Liu and R. H. Pletcher, "Compressibility and variable density effects in turbulent boundary layers," J. Heat Transfer **129**, 441-448 (2007).
[36] A. Walz, *Boundary Layers of Flow and Temperature* (MIT Press, 1969).
[37] T. Cebeci and A. M. O. Smith, *Analysis of Turbulent Boundary Layers* (Academic Press, 1974).
[38] J. Gaviglio, "Reynolds analogies and experimental study of heat transfer in the supersonic boundary layer," Int. J. Heat Mass Transfer **30**(5), 911-926 (1987).
[39] H. M. Nagib, K. A. Chauhan, and P. A. Monkewitz, "Approach to an asymptotic state for zero pressure gradient turbulent boundary layers," Philos. Trans. R. Soc. A **365**, 755-770 (2007).
[40] D. Wittich, S. Gordeyev, and E. Jumper, "Revised scaling of optical distortions caused by compressible, subsonic turbulent boundary layers," AIAA Paper No. 2007-4009, 2007.
[41] J. Cress, "Optical aberrations cause by coherent structures in a subsonic, compressible, turbulent boundary layer," Ph.D. thesis, University of Notre Dame, 2010.
[42] Q. Gao, S. Yi, Z. Jiang, L. He, and X. Wang, "Structure of the refractive index distribution of the supersonic turbulent boundary layer," Opt. Lasers Eng. **51**, 1113-1119 (2013).
[43] L. Duan and M. M. Choudhari, "Numerical study of pressure fluctuations due to a Mach 6 turbulent boundary layer," AIAA Paper No. 2013-0532, 2013.
[44] A. Smith, S. Gordeyev, T. Saxton-Fox, and B. McKeon, "Subsonic boundary-layer wavefront spectra for a range of Reynolds numbers," AIAA Paper No. 2014-2491, 2014.